CHEMISTRY OF MATERIALS

Article

pubs.acs.org/cm

Antimony-Doped Tin(II) Sulfide Thin Films

Prasert Sinsermsuksakul,[†] Rupak Chakraborty,[‡] Sang Bok Kim,[†] Steven M. Heald,[§] Tonio Buonassisi,[‡] and Roy G. Gordon*,[†]

[†]Department of Chemistry and Chemical Biology, Harvard University, Cambridge, Massachusetts 02138, United States

[‡]Department of Mechanical Engineering, Massachusetts Institute of Technology, Cambridge, Massachusetts 02139, United States

[§]Advanced Photon Source, Argonne National Laboratory, Argonne, Illinois 60439, United States

ABSTRACT: Thin-film solar cells made from earth-abundant, inexpensive, and nontoxic materials are needed to replace the current technologies whose widespread use is limited by their use of scarce, costly, and toxic elements.[1] Tin monosulfide (SnS) is a promising candidate for making absorber layers in scalable, inexpensive, and nontoxic solar cells. SnS has always been observed to be a *p*-type semiconductor. Doping SnS to form an *n*-type semiconductor would permit the construction of solar cells with *p*-*n* homojunctions. This paper reports doping SnS films with antimony, a potential *n*-type dopant. Small amounts of antimony (~1%) were found to greatly increase the electrical resistance of the SnS. The resulting intrinsic SnS(Sb) films could be used for the insulating layer in a *p*-*i*-*n* design for solar cells. Higher concentrations (~5%) of antimony did not convert the SnS(Sb) to low-resistivity *n*-type conductivity, but instead the films retain such a high resistance that the conductivity type could not be determined. Extended X-ray absorption fine structure analysis reveals that the highly doped films contain precipitates of a secondary phase that has chemical bonds characteristic of metallic antimony, rather than the antimony–sulfur bonds found in films with lower concentrations of antimony.

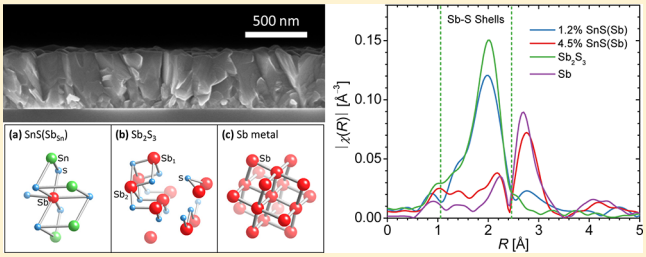

KEYWORDS: *thin films, doping, semiconductor, tin sulfide, antimony*

INTRODUCTION

In the past few decades, tin(II) sulfide (SnS) has gained much attention as a possible alternative absorber material for the next generation of thin-film solar cells to replace the current best-developed technology based on Cu(In,Ga)Se$_2$ and CdTe, which involve toxic Cd and rare elements In, Ga, and Te. In addition to low toxicity, low cost, and natural abundance of its constituent elements, SnS has high optical absorption ($\alpha > 10^4$ cm^{-1}) above the direct absorption edge at 1.3–1.5 eV.[2,3] It has native *p*-type conduction because of the small enthalpy of formation of tin vacancies, which generate shallow acceptors.[4] SnS-based heterojunction solar cells have been reported using different *n*-type partners such as ZnO,[5] CdS,[6] Cd$_{1-x}$Zn$_x$S,[7] SnS$_2$,[8] TiO$_2$,[9] and *a*-Si.[10] The power conversion efficiencies (η) achieved so far on these planar heterojunction devices are still rather low (<1.3%).[6] Some of the main contributors to this poor efficiency could be an unfavorable band offset and rapid carrier recombination at trap states near the interface between SnS and the *n*-type buffer layers.[11] In this aspect, a homojunction might provide a better device performance, provided that *n*-type SnS can be produced. In addition to the homojunction approach, improved SnS-based solar cells might have a *p*-*i*(SnS)-*n* structure, similar to a strategy proposed by Sites et al. for CdTe.[12] This approach requires SnS to have a low carrier concentration on the order of 10^{13} cm^{-3}, which is lower than typical undoped SnS values of 10^{15}–10^{18} cm^{-3}.[3,4,6,13] Therefore, the ability to control carrier concentration and conduction type of SnS could improve SnS-based thin film solar cells and, in general, could broaden the utility of SnS as an optoelectronic semiconductor outside the field of photovoltaics.

SnS can be doped by Ag[13,14] and Cu[15] to increase its hole concentration to around 10^{19} cm^{-3}. Dussan et al. attempted to use Bi to substitute Sn in SnS to provide *n*-type conduction, but the material remains *p*-type below 50% Bi concentration.[16] Sajeesh et al. reported *n*-type SnS thin films obtained by chemical spray pyrolysis, but this result is probably due to a significant *n*-type Sn$_2$S$_3$ impurity phase in the films.[17] One promising *n*-type substitutional dopant is antimony(III), Sb^{3+}, because of the similarity of its ionic radius to Sn^{2+}. Albers et al. reported the use of Sb as a dopant that lowers the hole concentration of SnS to be less than 10^{14} cm^{-3}.[13] Nonetheless, the specific Sb concentration and detailed studies of its effect on the electrical properties of SnS were not reported. By increasing the Sb concentration further, it might be possible to convert SnS to an *n*-type semiconductor. Here, we report the preparation of Sb-doped SnS thin films, SnS(Sb), from the reaction of bis(*N*,*N*′-diisopropylacetamidinato)tin(II) [Sn(MeC(N-*i*Pr)$_2$)$_2$] and tris(dimethylamido)antimony(III) [Sb(NMe$_2$)$_3$] with hydrogen sulfide (H$_2$S). We identify the dopant

Received: August 6, 2012
Revised: October 18, 2012
Published: November 15, 2012

chemical state, and report the effect of Sb dopant concentration on the crystal structure and electrical properties of the material.

EXPERIMENTAL SECTION

Sb-Doped SnS Thin Film. Pure, stoichiometric, single-phase SnS thin films can be obtained by atomic layer deposition (ALD) from the reaction of bis(*N*,*N*′-diisopropylacetamidinato)tin(II) [Sn(MeC(N-*i*Pr)$_2$)$_2$, referred here as Sn(amd)$_2$] and hydrogen sulfide (H_2S).[3] Rather than using ALD as previously reported,[3] SnS thin films were deposited using a modified chemical vapor deposition (CVD) process, referred here as a pulsed-CVD, to speed up the deposit rate to ∼15 times higher than that of ALD. The sequence of one cycle of a pulsed-CVD is composed of *(i)* injection of Sn(amd)$_2$ vapor using N_2 assistance, *(ii)* injection of H_2S gas to mix and react with the Sn(amd)$_2$ vapor trapped inside the deposition zone, and *(iii)* evacuation of the gas mixture and byproducts. Unlike conventional ALD, there is no purging of excess Sn(amd)$_2$ before H_2S injection, thereby increasing the deposition rate at the cost of some nonuniformity in the film thickness along the length of the reactor. The substrate temperature was set to 200 °C. The tin precursor source was kept at 95 °C. A gas mixture of 4% H_2S in N_2 (Airgas Inc.) was used as the source of sulfur. H_2S is a toxic, corrosive, and flammable gas (lower flammable limit of 4%).[18] Thus, it should be handled with caution. An appropriate reactor design for H_2S compatibility can be found elsewhere.[19] The partial pressures of Sn(amd)$_2$ and H_2S after injecting into the deposition zone for each pulsed-CVD cycle are approximately 100 mTorr and 240 mTorr, respectively.

Sb_2S_3 thin films can be prepared from ALD using the reaction of tris(dimethylamido)antimony(III) [Sb(NMe$_2$)$_3$] (Sigma-Aldrich) and hydrogen sulfide.[20] The stop-flow ALD mode[21,22] was used for the deposition. The antimony source was kept at room temperature (25 °C). The total exposure of Sb(NMe$_2$)$_3$ and H_2S for each of an ALD cycle were approximately 0.7 and 1.1 Torr·s, respectively. Sb-doped SnS thin films were deposited by inserting cycles of ALD Sb_2S_3 into the deposition of SnS. By varying the ratio between the numbers of Sb_2S_3 and SnS cycles, controlled concentrations of Sb^{3+} in SnS can be obtained. For example, a 1% cycle ratio film, SnS(1% Sb), was prepared by alternating between 99 cycles of SnS and 1 cycle of Sb_2S_3. Three samples were deposited using 1%, 2%, and 5% Sb cycles to determine the effect of Sb concentration on the crystal structure and electrical properties of the films.

Material Characterization. Film morphology was characterized using field-emission scanning electron microscopy (FESEM, Zeiss, Ultra-55). The film thickness was determined from cross-sectional SEM. The elemental composition of the films was determined by Rutherford backscattering spectroscopy (RBS, Ionex 1.7 MV Tandetron) and time-of-flight secondary ion mass spectroscopy (ToF-SIMS). X-ray photoelectron spectroscopy (XPS, Surface Science, SSX-100) was used to detect possible carbon, nitrogen, and oxygen contamination in the films. The crystal structures of SnS and Sb-doped SnS thin films were examined by X-ray diffraction (XRD, PANalytical X'Pert Pro) with Cu Kα radiation (λ = 1.542 Å) using θ-2θ scan. The lattice parameters were calculated from least-squares fitting to the position of the Bragg peaks determined by Gaussian fit. Electrical properties of the films were characterized by Hall measurement (MMR technologies K2500) using the Van der Pauw method at 300 K. Synchrotron-based extended X-ray absorption fine structure (EXAFS) was used to study the local atomic environment of the antimony dopant. Synchrotron measurements were conducted at beamline 20-BM at the Advanced Photon Source of Argonne National Laboratory.[23]

RESULTS AND DISCUSSION

The obtained SnS and Sb-doped SnS films appeared smooth, pinhole free, and adhere well to the substrate (a-SiO_2). Figure 1 shows the surface morphology of an undoped SnS film and a SnS(5% Sb) film grown by pulsed-CVD at 200 °C, as observed by SEM. Because of the low level of doping, the surface

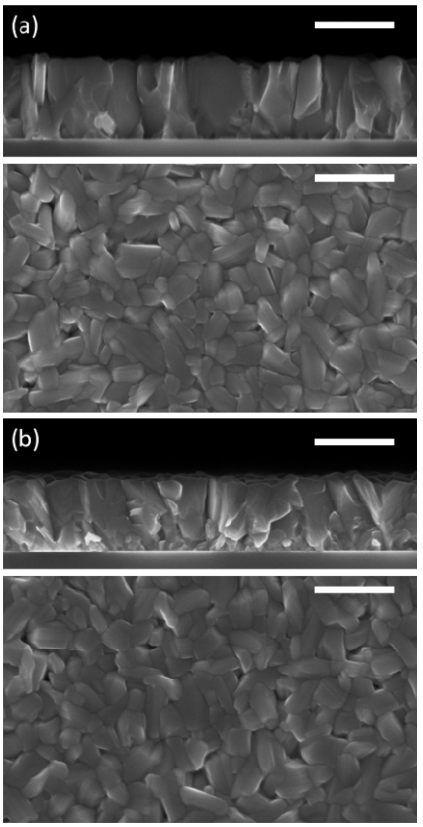

Figure 1. Cross-sectional and plan-viewed SEM images of (a) an undoped SnS film and (b) a SnS(5% Sb) film. The scale bar is 500 nm.

morphology of undoped SnS and all of the Sb-doped SnS samples are not significantly different. The film thicknesses of all the samples are approximately 500 nm, as determined from cross-sectional SEM. The chemical composition of the undoped SnS film was measured using RBS to be stoichiometric SnS to within the detection limit (±1%). As in ALD SnS[3] and ALD Sb_2S_3,[20] XPS does not detect any carbon or nitrogen contamination in the Sb-doped SnS films deposited at this particular temperature.

The atomic concentration of Sb in SnS was estimated by ToF-SIMS (Figure 2**a**) from the average intensity of Sb^+ and Sn^+ using a Cs^+ sputter source. If the efficiencies of generating Sb^+ and Sn^+ ions are assumed to be the same, then the Sb concentrations in SnS(1% Sb), SnS(2% Sb), and SnS(5% Sb) are determined to be 0.7 ± 0.2%, 1.2 ± 0.3%, and 4.5 ± 0.3%, respectively. Because we lack absolute concentration standards for SIMS analysis of dilute Sb in Sn, these concentrations could be in error by a constant calibration factor. Because of the chemical similarity of tin and antimony metals, it is expected that the calibration factor should not deviate significantly from unity.

From Figure 2**b**, a slight deviation from linearity between the Sb concentration and Sb growth cycle percentage was observed in the SnS(5% Sb) sample. If the reactivity of Sb(III) precursor and H_2S was identical on SnS and SnS(x% Sb) surfaces, then the atomic concentrations of Sb would be linearly proportional to their respective cycle percentages. However, the reactivities and chemisorptions on different surfaces, in general, are not the same. Thus, the actual Sb concentrations may not be exactly proportional to the cycle ratios, as observed in this case. This

dx.doi.org/10.1021/cm3024988 | *Chem. Mater.* 2012, 24, 4556−4562

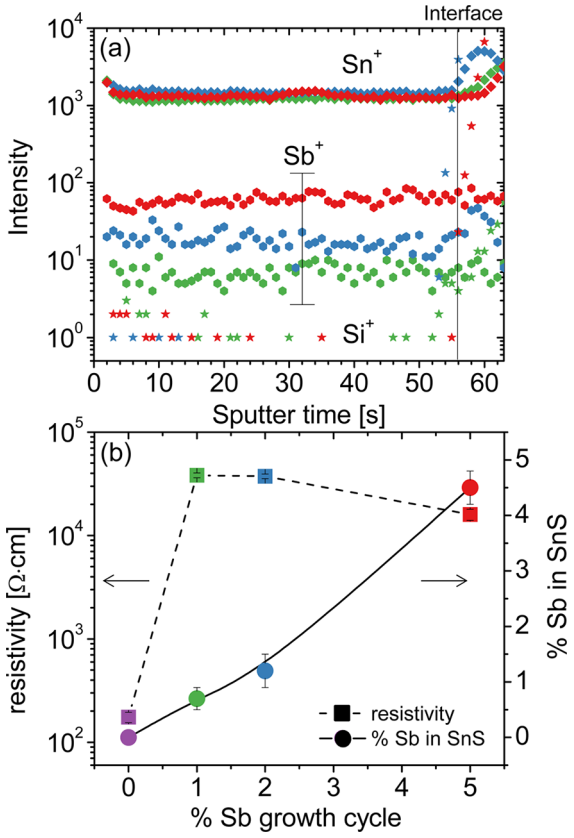

Figure 2. (**a**) ToF-SIMS of Sb-doped SnS films at 1%, 2%, and 5% Sb growth cycle. (**b**) Film resistivity and Sb concentration in SnS determined from ToF-SIMS as a function of the % Sb growth cycle.

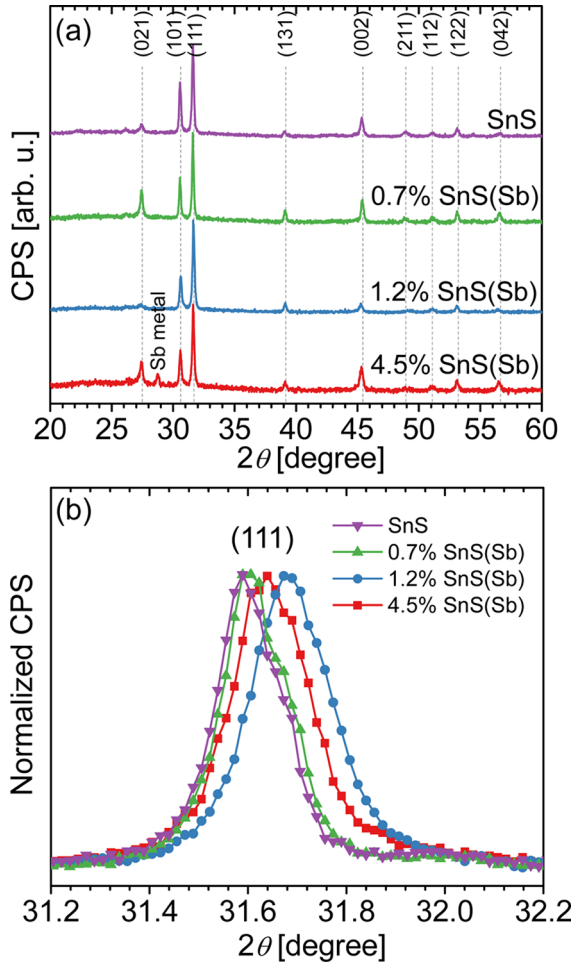

Figure 3. (**a**) XRD spectra of SnS and 0.7%, 1.2%, and 4.5% Sb-doped SnS. (**b**) An expansion around (111) lattice plane showing changes in lattice constants after Sb-doping.

phenomenon was also observed in other doping systems, such as Al doped into ZnO,[24] TiO_2,[25] and SnO_2.[26]

Figure 3**a** shows the X-ray diffraction (XRD) patterns of SnS and Sb-doped SnS films, which correspond to the orthorhombic structure of Herzenbergite SnS (PDF No. 00-039-0354, a = 4.3291 Å, b = 11.1923 Å, c = 3.9838 Å). Other impurity phases (i.e., Sn_2S_3 and SnS_2) were not detected in the deposited films. At 4.5% Sb-concentration, one Bragg peak at $2\theta = 28.7°$ was observed, but this peak does not belong to the known SnS or Sb_2S_3 phases. The peak could be assigned to the (040) plane of Valentinite Sb_2O_3 (PDF No. 01-072-2738) or the (012) plane of rhombohedral Sb (PDF No. 00-035-0732). However, depth profiling XPS reveals no oxygen contamination in this sample. Thus, this Bragg peak is most likely due to Sb; presumably, the concentration of Sb in this sample exceeded the solid solubility at deposition temperature (or upon cooling); the resulting supersaturation was relieved via precipitation of a secondary phase. Figure 3**b** presents the XRD in the region near the (111) lattice plane. Since the Bragg angle θ is inversely proportional to the lattice spacing d, which for the (111) plane equals to $[abc][(ab)^2 + (bc)^2 + (ac)^2]^{-1/2}$ where a, b, and c are lattice constants, the shift of the (111) peak position to the higher θ value indicates the crystal lattice shrinkage after Sb-doping. This unit cell volume decreases with increasing Sb concentration from 0.7% to 1.2% probably because of substitution of smaller Sb^{3+} for Sn^{2+}, but increases less with higher (4.5%) doping because of the precipitation of the secondary phase, as we shall see by correlating these results with EXAFS.

Table 1 shows some electrical properties of SnS and Sb-doped SnS thin films at 300 K. The undoped SnS thin film shows resistivity of 175 Ω cm, hole concentration of 4.4×10^{15} cm^{-3}, and mobility of 8 cm^2 V^{-1} s^{-1}. The addition of small amounts of Sb, even at 0.7% concentration, effectively produces an insulating film with resistivity increased to 3.82×10^4 Ω cm, more than 2 orders of magnitude higher than the undoped film. Upon increasing Sb concentration up to 1.2%, the resistivity of Sb-doped SnS film remains roughly the same, 3.74×10^4 Ω cm. However, the film resistivity drops by half to 1.60×10^4 Ω cm when the Sb concentration increases up to 4.5%. Unfortunately, the carrier concentration and conductivity type of the Sb-doped SnS films cannot be measured from the current Hall setup because of their high resistivities.

To clarify the mechanism behind the anomalous rise and fall of SnS film resistivity with increasing Sb doping concentration, we performed Extended X-ray Absorption Fine Structure (EXAFS) measurements at the Sb edge. The EXAFS technique is sensitive to the local atomic environment surrounding the dopant atoms, elucidating the chemical state of the dopant atoms (e.g., substitutional, interstitial, or second-phase particle). EXAFS was performed at the Sb−K_α X-ray absorption edge on the 1.2% SnS(Sb) film, the 4.5% SnS(Sb) film, the Sb_2S_3 film, and an Sb metal reference standard. We also performed EXAFS on the 0.7% SnS(Sb) film, but the signal was too weak to obtain a high-quality EXAFS spectrum. Data were analyzed using

dx.doi.org/10.1021/cm3024988 | Chem. Mater. 2012, 24, 4556−4562

Table 1. Summary of Sb Concentrations, Lattice Constants, and Electrical Properties of Undoped and Sb-Doped SnS Films

sample	cycle ratio Sn:Sb	%Sb in SnS	lattice constant (Å)			resistivity (Ω cm)	carrier density (cm^{-3})	mobility ($cm^2/(V\ s)$)
			a	*b*	*c*			
SnS	1:0	0	4.30 ± 0.01	11.19 ± 0.02	3.99 ± 0.01	175	$+4.4 \times 10^{15}$	8
SnS(1% Sb)	99:1	0.7 ± 0.2	4.30 ± 0.01	11.19 ± 0.02	3.99 ± 0.01	3.82×10^4		
SnS(2% Sb)	49:1	1.2 ± 0.3	4.27 ± 0.01	11.17 ± 0.02	3.99 ± 0.01	3.74×10^4	below measurement sensitivity	
SnS(5% Sb)	19:1	4.5 ± 0.3	4.28 ± 0.01	11.19 ± 0.02	3.99 ± 0.01	1.60×10^4		

standard EXAFS analysis procedures[27] to obtain the Fourier transforms of the EXAFS spectra shown in Figure 4. All spectra

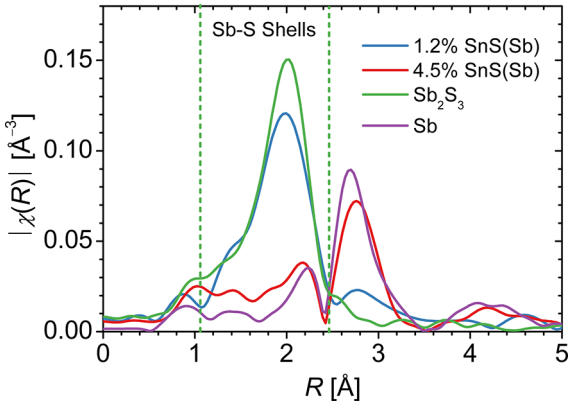

Figure 4. Summary of EXAFS measurements: The magnitude of the complex Fourier transform of $\chi(k)$ at the Sb edge of the 1.2% SnS(Sb) film, 4.5% SnS(Sb) film, Sb_2S_3 film, and Sb metal standard. The peak at 2 Å in the Sb_2S_3 data is due to sulfur nearest-neighbors of antimony.

were *k*-weighted by 1, and the transform ranges for each of the spectra were 3.15−9, 3−10.6, 3.3−12.2, and 2.75−15 $Å^{-1}$, respectively. In Figure 4, the peak at 2 Å of the 1.2% SnS(Sb) Fourier transformed EXAFS spectrum matches well with that of the Sb_2S_3 spectrum. In Sb_2S_3, this peak is due to the sulfur nearest neighbors of antimony, suggesting that the antimony in the 1.2% SnS(Sb) sample may be incorporated into the film in a sulfur environment. In contrast, the Fourier transformed EXAFS spectrum of the 4.5% SnS(Sb) shows close resemblance to that of Sb metal, implying that the antimony in the 4.5% SnS(Sb) may be present in an antimony environment.

To elucidate the precise chemical states of Sb dopants in SnS films, EXAFS spectra were modeled using the Artemis interface to the IFEFFIT software package.[28] In the 1.2% SnS(Sb) film, antimony may either be incorporated into the film as an Sb_{Sn} substitution as desired, or as Sb_2S_3 second-phase particles. For this reason, we evaluated both structural models: (a) a 6-shell model of SnS with the Sb_{Sn} substitution at the central atom, denoted by SnS(Sb_{Sn}); (b) a 4-shell model of Sb_2S_3 with the two distinct lattice sites of Sb in Sb_2S_3 weighted equally. For the 4.5% SnS(Sb) film, we evaluated a 2-shell model of Sb metal. Figure 5 gives a spatial representation of each structural model. The paths used in each model are outlined in Table 2. The refinements were performed using 6−10 free parameters, including the half-path lengths δR_i, their mean square variation σ_i^2, the relaxation term S_0^2, and energy offset E_0, with 8−12 independent points per data set.

The refinements of models (a) and (b) achieved good fits (R = 1.5% and R = 1.7%, respectively) for the 1.2% SnS(Sb) data, while the refinement of model (c) achieved a good fit (R = 3.4%) for the 4.5% SnS(Sb) data. Figure 6 shows these EXAFS

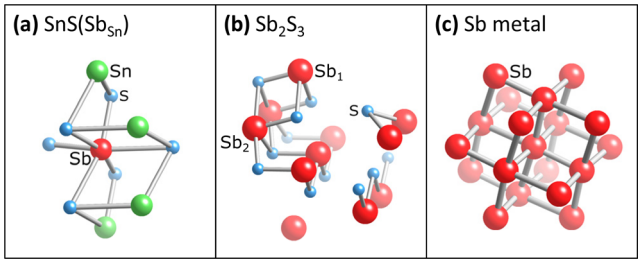

Figure 5. Ball-and-stick representation of (**a**) SnS with the Sb_{Sn} substitution at the central atom, (**b**) Sb_2S_3, and (**c**) Sb metal. Green: Sn; Blue: S; Red: Sb. For clarity, the cluster sizes shown are smaller than those used for EXAFS fitting. Note the two distinct lattice sites of Sb in Sb_2S_3, the trivalent Sb_1 and quintvalent Sb_2. Nearest-neighbor distances are given in Table 2.

Table 2. Path Names for Each Structure Model with Corresponding Half-Path Lengths and Coordination Numbers[a]

structure model								
SnS(Sb_{Sn}) (a)			Sb_2S_3 (b)			Sb metal (c)		
path	R_{eff} (Å)	*N*	path	R_{eff} (Å)	*N*	path	R_{eff} (Å)	*N*
S_1	2.6237	1	$[Sb_1] - S_3$	2.5044	1	Sb_2	2.9063	3
S_2	2.6658	2	$[Sb_1] - S_2$	2.5225	2	Sb_3	3.3513	3
S_3	3.2908	2	$[Sb_2] - S_1$	2.3836	1			
S_4	3.3908	1	$[Sb_2] - S_3$	2.6747	2			
Sn_1	3.4937	2						
Sn_2	3.9870	2						

[a]All paths are single-scattering events with Sb as the atom of origin. For model (b), the atom of origin is shown in brackets to distinguish between the two distinct lattice sites of Sb in Sb_2S_3, denoted by Sb_1 and Sb_2.

data and fits, and Figure 7 shows the real parts and magnitudes of the Fourier transform of these data. Table 3 gives the best-fit values of parameters for the fitted spectra. Attempts to refine model (c) for the 1.2% SnS(Sb) data or models (a) and (b) for the 4.5% SnS(Sb) data were not possible with R values under 60%. The Sb substitutional [SnS(Sb_{Sn})] model qualitatively gives the best fit for the 1.2% SnS(Sb) data, closely matching the phase and amplitude of $\chi(R)$ beyond the sulfur shells. Although the Sb_2S_3 model also fits reasonably well to the data, formation of the Sb_2S_3 phase is unsupported by XRD of the 1.2% SnS(Sb) film. Peaks corresponding to Sb_2S_3 were not observed in the XRD pattern, and the SnS lattice constant shift indicates an incorporation of Sb into the SnS lattice. Furthermore, the phase composition of the SnS-Sb system as measured by Kurbanova et al. includes only the SnS and Sb phases for temperatures of 30−500 °C.[29] For these reasons, we believe that antimony is predominantly acting as a substitutional dopant in the 1.2% SnS(Sb), causing the observed increase in resistivity. However, we cannot rule out the

dx.doi.org/10.1021/cm3024988 | Chem. Mater. 2012, 24, 4556−4562

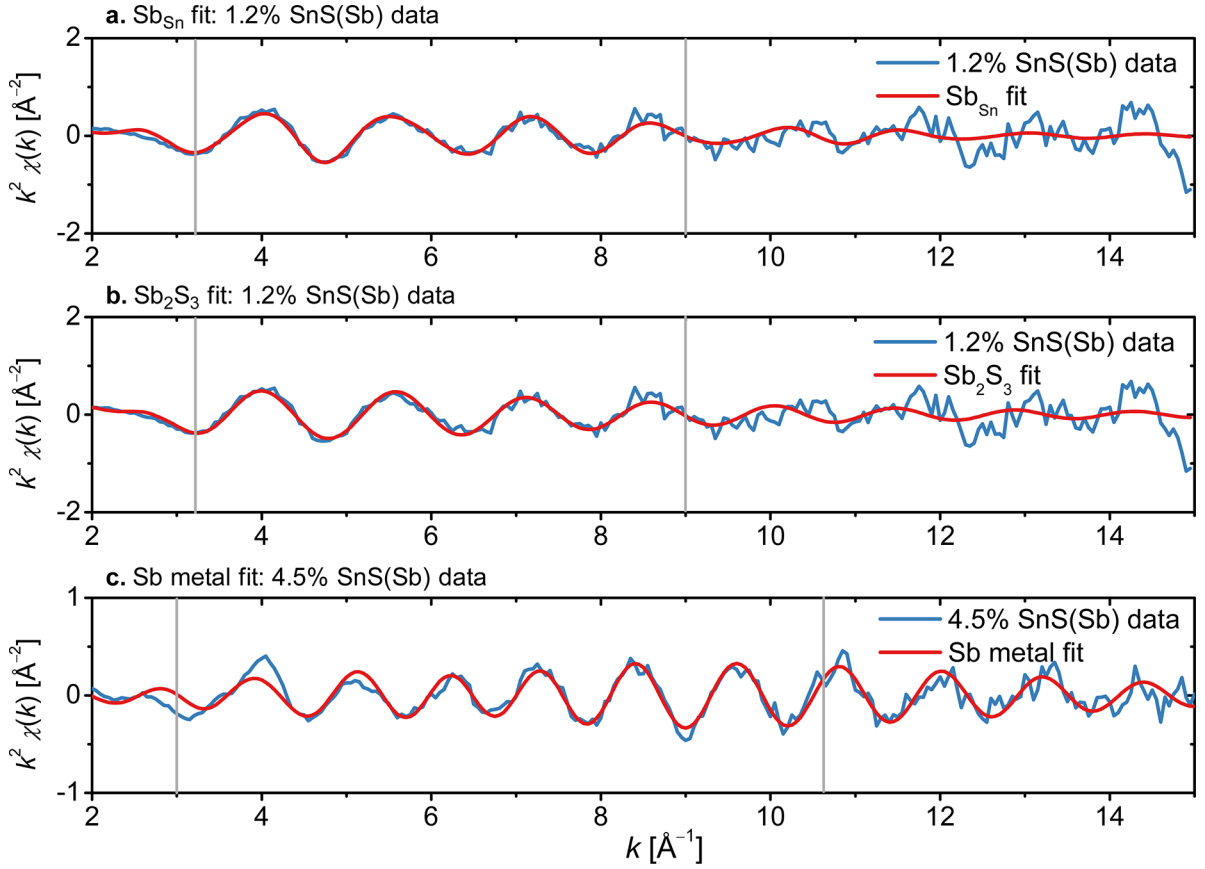

Figure 6. EXAFS data and fits for Sb edge: (a) 1.2% SnS(Sb) data with SnS(Sb$_{Sn}$) fit, (b) 1.2% SnS(Sb) data with Sb_2S_3 fit, and (c) 4.5% SnS(Sb) data with Sb metal fit. The vertical lines denote the range chosen for Fourier transformation.

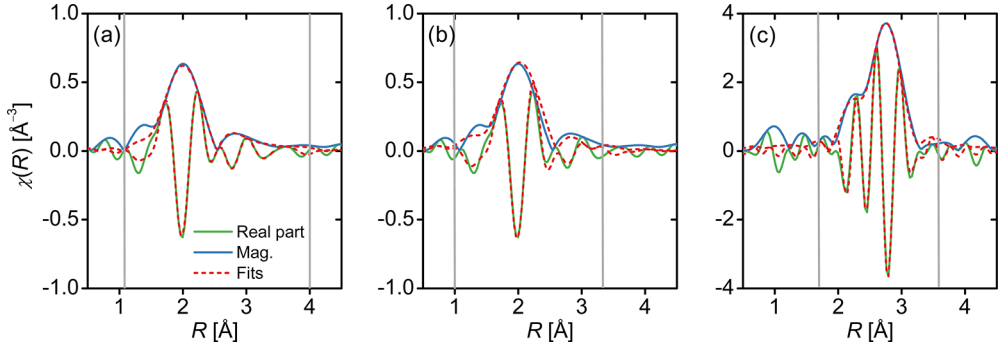

Figure 7. Real part and magnitude of Fourier transformed EXAFS data and fits: (a) 1.2% SnS(Sb) data with SnS(Sb$_{Sn}$) fit, (b) 1.2% SnS(Sb) data with Sb_2S_3 fit, and (c) 4.5% SnS(Sb) data with Sb metal fit. The vertical lines denote the fitting range.

possibility that a small fraction of Sb exists in the Sb_2S_3 phase, falling below the sensitivity of XRD.

The Sb metal model matches well with the 4.5% SnS(Sb) EXAFS data. This supports our hypothesis that the antimony in the 4.5% SnS(Sb) is present predominantly in a secondary phase, consistent both with our XRD observation of a new peak emerging with high doping density, and with the aforementioned phase composition study of the SnS-Sb system.[29] The formation of Sb metal observed by EXAFS may underlie the decrease of resistivity at the highest Sb doping level; since the majority of dopant atoms in this film do not occupy substitutional lattice sites, the degree of compensation is reduced, and the free hole concentration is increased. We also note that dopant precipitation into metallic nanoparticles has been observed for other systems such as metal-doped ZnO.[30,31]

CONCLUSION

In conclusion, Sb-doped SbS thin films were deposited by pulsed-CVD using the reaction of Sn(MeC(N-*i*Pr)$_2$)$_2$ and Sb(NMe$_2$)$_3$ with H_2S. Small amounts of Sb (~1%) in SnS increase the film resistivity by more than 2 orders of magnitude, most likely due to substitutional doping. Sb addition at low levels is an effective means of producing compensated, insulating SnS films, which could be useful in solar cells with a *p-i-n* heterostructure. The conductivity type of the Sb-doped SnS films could not be determined because of their high resistivity. Increasing the doping level from 1.2% to 4.5% appears to cause clustering of the Sb into metallic precipitates.

dx.doi.org/10.1021/cm3024988 | *Chem. Mater.* 2012, 24, 4556–4562

Table 3. Best-Fit EXAFS Parameters and Corresponding Paths for Three Structure Models[a]

	structure model					
	SnS(Sb_{Sn}) [(a)]		Sb_2S_3 [(b)]		Sb [(c)]	
parameters	values	path	values	path	values	path
E_0	10.2 (2.7)	all paths	10.6 (1.0)	all paths	9.9 (2.3)	all paths
S_0^2	0.82 (0.05)	all paths	0.93 (0.10)	all paths	0.77 (0.25)	all paths
δR_1	−0.15 (0.02)	S_1	0.02 (24.7)	$[Sb_1] - S_3$	0.00069 (0.017)	Sb_2
δR_2	δR_1	S_2	0.0002 (2.8)	$[Sb_1] - S_2$	0.0032 (0.060)	Sb_3
δR_3	0.050 (0.089)	S_3	−0.01 (0.07)	$[Sb_2] - S_1$		
δR_4	0.21 (0.35)	S_4	−0.16 (0.36)	$[Sb_2] - S_3$		
δR_5	−0.08 (0.11)	Sn_1				
δR_6	−0.26 (0.13)	Sn_2				
σ_1^2	0.0052 (0.0020)	S_1	0.003	$[Sb_1] - S_3$	0.0051 (0.0024)	Sb_2
σ_2^2	σ_1^2	S_2	σ_1^2	$[Sb_1] - S_2$	0.019 (0.011)	Sb_3
σ_3^2	0.011 (0.022)	S_3	0.0063(0.0072)	$[Sb_2] - S_1$		
σ_4^2	σ_3^2	S_4	0.0056 (0.0031)	$[Sb_2] - S_3$		
σ_5^2	0.014 (0.039)	Sn_1				
σ_6^2	σ_5^2	Sn_2				

[a]Models (a) and (b) are fit to 1.2% SnS(Sb) data, and model (c) is fit to 4.5% SnS(Sb) data. See Table 1 for path details.

AUTHOR INFORMATION

Corresponding Author

*Tel: (617)-495-4017. Fax: (617)-495-4723. E-mail: gordon@chemistry.harvard.edu.

Notes

The authors declare no competing financial interest.

ACKNOWLEDGMENTS

We acknowledge Y. Segal for his contributions at the synchrotron beamline and his initial interpretations of the data. We also thank K. Hartman for her initial support in processing and analyzing the data. This work was supported by the U.S. Department of Energy SunShot Initiative under Contract No. DE-EE0005329, by the U.S. National Science Foundation under grant No. CBET-1032955, and by Saint Gobain S. A., which also supplied the SIMS analyses. P.S. appreciates the support from the Development and Promotion of Science and Technology Talents Project (DPST), Thailand. R.C. acknowledges the support of a National Science Foundation Graduate Research Fellowship. This work was performed in part at the Center for Nanoscale Systems (CNS), a member of the National Nanotechnology Infrastructure Network (NNIN), which is supported by the National Science Foundation under NSF award No. ECS-0335765. Use of the Advanced Photon Source, an Office of Science User Facility operated for the U.S. Department of Energy (DOE) Office of Science by Argonne National Laboratory, was supported by the U.S. DOE under Contract No. DE-AC02-06CH11357.

REFERENCES

(1) Wadia, C.; Alivisatos, A. P.; Kammen, D. M. *Environ. Sci. Technol.* **2009**, *43* (6), 2072−2077.

(2) Mathews, N. R.; Anaya, H. B. M.; Cortes-Jacome, M. A.; Angeles-Chavez, C.; Toledo-Antonio, J. A. *J. Electrochem. Soc.* **2010**, *157* (3), H337−H341.

(3) Sinsermsuksakul, P.; Heo, J.; Noh, W.; Hock, A. S.; Gordon, R. G. *Adv. Energy Mater.* **2011**, *1* (6), 1116−1125.

(4) Vidal, J.; Lany, S.; d'Avezac, M.; Zunger, A.; Zakutayev, A.; Francis, J.; Tate, J.. *Appl. Phys. Lett.* **2012**, *100*, (3).

(5) Ghosh, B.; Das, M.; Banerjee, P.; Das, S. *Semicond. Sci. Technol.* **2009**, *24*, (2).

(6) Reddy, K. T. R.; Reddy, N. K.; Miles, R. W. *Sol. Energy Mater. Sol. Cells* **2006**, *90* (18−19), 3041−3046.

(7) Gunasekaran, M.; Ichimura, M. *Sol. Energy Mater. Sol. Cells* **2007**, *91* (9), 774−778.

(8) Sanchez-Juarez, A.; Tiburcio-Silver, A.; Ortiz, A. *Thin Solid Films* **2005**, *480*, 452−456.

(9) Wang, Y.; Gong, H.; Fan, B. H.; Hu, G. X. *J. Phys. Chem. C* **2010**, *114* (7), 3256−3259.

(10) Jiang, F.; Shen, H. L.; Wang, W.; Zhang, L. *J. Electrochem. Soc.* **2012**, *159* (3), H235−H238.

(11) Sugiyama, M.; Reddy, K. T. R.; Revathi, N.; Shimamoto, Y.; Murata, Y. *Thin Solid Films* **2011**, *519* (21), 7429−7431.

(12) Sites, J.; Pan, J. *Thin Solid Films* **2007**, *515* (15), 6099−6102.

(13) Albers, W.; Vink, H. J.; Haas, C.; Wasscher, J. D. *J. Appl. Phys.* **1961**, *32*, 2220.

(14) Devika, M.; Reddy, N. K.; Ramesh, K.; Gunasekhar, K. R.; Gopal, E. S. R.; Reddy, K. T. R. *J. Electrochem. Soc.* **2006**, *153* (8), G727−G733.

(15) Zhang, S. A.; Cheng, S. Y. *Micro Nano Lett.* **2011**, *6* (7), 559−562.

(16) Dussan, A.; Mesa, F.; Gordillo, G. *J. Mater. Sci.* **2010**, *45* (9), 2403−2407.

(17) Sajeesh, T. H.; Warrier, A. R.; Kartha, C. S.; Vijayakumar, K. P. *Thin Solid Films* **2010**, *518* (15), 4370−4374.

(18) *Hydrogen Sulfide*; Airgas Inc: Radnor, PA, 2010; MSDS No.001029.

(19) Dasgupta, N. P.; Mack, J. F.; Langston, M. C.; Bousetta, A.; Prinz, F. B. *Rev. Sci. Instrum.* **2010**, *81*, 4.

(20) Yang, R. B.; Bachmann, J.; Reiche, M.; Gerlach, J. W.; Gosele, U.; Nielsch, K. *Chem. Mater.* **2009**, *21* (13), 2586−2588.

(21) Karuturi, S. K.; Liu, L. J.; Su, L. T.; Zhao, Y.; Fan, H. J.; Ge, X. C.; He, S. L.; Yoong, A. T. I. *J. Phys. Chem. C* **2010**, *114* (35), 14843−14848.

(22) Heo, J.; Hock, A. S.; Gordon, R. G. *Chem. Mater.* **2010**, *22* (17), 4964−4973.

(23) Heald, S.; Stern, E.; Brewe, D.; Gordon, R.; Crozier, D.; Jiang, D. T.; Cross, J. *J. Synchrotron Radiat.* **2001**, *8*, 342−344.

(24) Na, J. S.; Peng, Q.; Scarel, G.; Parsons, G. N. *Chem. Mater.* **2009**, *21* (23), 5585−5593.

(25) Kim, S. K.; Choi, G. J.; Kim, J. H.; Hwang, C. S. *Chem. Mater.* **2008**, *20* (11), 3723−3727.

(26) Heo, J.; Liu, Y. Q.; Sinsermsuksakul, P.; Li, Z. F.; Sun, L. Z.; Noh, W.; Gordon, R. G. *J. Phys. Chem. C* **2011**, *115* (20), 10277−10283.

(27) Sayers, D. E.; Bunker, B. A. In *X-Ray Absorption: Basic Principles of EXAFS, SEXAFS and XANES*; Koningsberger, D. C., Prins, R., Eds.; Wiley: New York, 1988; p 211.
(28) Ravel, B.; Newville, M. *J. Synchrotron Radiat.* **2005**, *12*, 537−541.
(29) Kurbanova, R. D.; Movsumzade, A. A.; Allazov, M. R. *Inorg. Mater.* **1987**, *23* (11), 1585−1587.
(30) Heald, S. M.; Kaspar, T.; Droubay, T.; Shutthanandan, V.; Chambers, S.; Mokhtari, A.; Behan, A. J.; Blythe, H. J.; Neal, J. R.; Fox, A. M.; Gehring, G. A. *Phys. Rev. B* **2009**, *79*, (7).
(31) Fons, P.; Yamada, A.; Iwata, K.; Matsubara, K.; Niki, S.; Nakahara, K.; Takasu, H. *Nucl. Instrum. Methods Phys. Res., Sect. B* **2003**, *199*, 190−194.